



# Quantitative photocatalyzed soot oxidation on titanium dioxide

Paul Chin<sup>1</sup>, Christine S. Grant, David F. Ollis<sup>\*</sup>

Department of Chemical and Biomolecular Engineering, North Carolina State University, Box 7905, Raleigh, NC 27695-7905, USA

## ARTICLE INFO

### Article history:

Received 28 June 2008

Received in revised form 2 September 2008

Accepted 3 September 2008

Available online 1 October 2008

### Keywords:

Titania

Photocatalysis

Soot

Kinetic model

Oxidation

Formal quantum efficiency

## ABSTRACT

We report here the titanium dioxide (TiO<sub>2</sub>) photocatalyzed oxidation of deposited hurricane lamp soot. Sol-gel derived TiO<sub>2</sub> was coated on quartz crystal microbalance (QCM) elements. Characterization by spectroscopic ellipsometry (SE) and atomic force microscopy (AFM) revealed low surface roughness of 0–17%, and SE showed a linear variation of the TiO<sub>2</sub> thickness versus the number of sol-gel spin coats.

Soot was deposited on the calcined TiO<sub>2</sub> film using an analytical rotor passing through a hurricane lamp flame, and subsequently irradiated with near-UV light. Varying the soot mass on the TiO<sub>2</sub>-coated QCM crystals revealed behaviors over 20,000 min ranging from total soot destruction of a single pass soot layer to minimal oxidation of an eight pass soot layer, the latter caused by soot screening of the incident UV light. A series/parallel reaction mechanism [P. Chin, G.W. Roberts, D.F. Ollis, *Industrial & Engineering Chemistry Research* 46 (2007) 7598] developed to describe previous literature data on TiO<sub>2</sub>-catalyzed soot photooxidation was successfully employed to capture the longer time changes in presumably graphitic soot mass as a function of UV illumination time from 1000 to 20,000 min and of soot layer thickness. Short time soot mass loss is attributed to oxidation of organic carbons deposited on the graphitic soot components. This kinetic model can be used to predict the rate of TiO<sub>2</sub>-catalyzed soot destruction as a function of near-UV illumination time and initial soot layer thickness.

© 2008 Elsevier B.V. All rights reserved.

## 1. Introduction

The development of “self-cleaning” surfaces of glass [1–3], tile [4], and other exterior material [5] using TiO<sub>2</sub> photocatalytic oxidation (PCO) logically demands consideration of likely organic deposits, including soot. To date, four articles have addressed TiO<sub>2</sub> PCO of soot [6–9], but only two reported quantitative data [6,7] and no substantive kinetic model was proposed. We have generated two soot kinetic models [9] to describe mass loss data of Lee and Choi [6] and CO<sub>2</sub> generation data of Mills et al. [7]. A comparison of the two studies reveals that although both research groups examined the TiO<sub>2</sub> PCO of “soot,” the large differences in fitted parameter values [9] show that soot characteristics affect the kinetic rate constants and molar absorptivity of such deposits.

The soot composition is categorized primarily as three components [10–14]: (a) graphitic or inorganic carbon; (b) organic carbon, such as unburned hydrocarbons (HCs), soluble organic fractions (SOFs), or volatile organic fractions (VOFs); and (c) inorganic material (e.g., sulfates, water, ash), especially in diesel

soot. We explore here only the first two components, organic and graphitic, by use of soot formed in a hurricane lamp flame. The organic carbons can constitute a significant portion of the total soot; for example, fuel SOFs can represent 20–25% of the particulate emissions in diesel engine exhaust [11,15]. The organic carbons may be removed thermally from the soot surface, in contrast to the graphitic carbon. Temperature-programmed desorption (TPD) experiments by Ahlström and Odenbrand [14] and Querini et al. [16] confirmed hydrocarbon removal from diesel soot at temperatures from 200 to 400 °C and below 300 °C, respectively. The organic carbons are assumed to surround and fill the micropores of graphitic carbon [12]. Electron microscope images of soot particles reveal the porous nature of soot [17–19]. Ahlström and Odenbrand [14] observed an increase in the BET specific area of diesel soot from 35 to 270 m<sup>2</sup>/g as the sample degassing (N<sub>2</sub>) temperature increased from 100 to 600 °C. They attributed this increase to desorption of water and volatile unburned HCs from the soot.

For our model development, we summarize the earlier literature on a related process, the thermal catalytic oxidation of soot, which exhibits different reaction rates for the organic and graphitic portions of soot carbons [13,15,20–23]. Neef et al. [20] observed high reaction rates for the initial 10–20% soot conversion compared to later reaction times for both diesel soot and Degussa Printex-U, a carbon black often used as a model soot. They ascribe

<sup>\*</sup> Corresponding author. Tel.: +1 919 515 2329 fax: +1 919 515 3465.

E-mail addresses: [paul.chin@mac.com](mailto:paul.chin@mac.com) (P. Chin), [grant@eos.ncsu.edu](mailto:grant@eos.ncsu.edu) (C.S. Grant), [ollis@eos.ncsu.edu](mailto:ollis@eos.ncsu.edu) (D.F. Ollis).

<sup>1</sup> Present address: TIAx LLC, 15 Acorn Park, Cambridge, MA 02140-2301, USA.

the fast reaction to oxidation of the more reactive compounds, such as adsorbed hydrocarbons. Research by de Soete [21] displayed faster oxidation of *n*-hexadecane and  $\alpha$ -ethylnaphthalene soots than of their char counterparts, where the char is produced by thermal desorption of the volatiles in the initial soot under  $N_2$  atmosphere at 1100 °C. The char SOFs are more than an order of magnitude lower than those for the original soot. Ahlström and Odenbrand [23] plotted the ratio of combustion rates for degassed (600 °C,  $N_2$ , 1 h) to fresh diesel soot and noted a ratio of 0.4 for temperatures lower than 350 °C. The lowered combustion rate after sample degassing pretreatment was caused by the lack of unburned HCs. Neri et al. [13] tested various metal oxide catalysts and determined  $Fe_2O_3$  to be a better HC oxidation catalyst than  $V_2O_5$  and CuO, while the latter catalysts were better for inorganic carbon oxidation compared to non-catalyzed soot oxidation. They suggested that in the presence of a thermal catalyst, HCs are more readily combusted than graphitic carbon. Darcy et al. [22] developed a diesel soot oxidation reaction rate model consisting of a “fast” oxidation of VOFs and a “slow” oxidation of the less reactive (i.e., inorganic carbon) soot portion. Their model was successfully applied to both catalyzed and non-catalyzed soot oxidation data. Finally, Messerer et al. [15] used a pseudo-first order rate equation to describe their non-catalyzed diesel soot oxidation over a range of 275–450 °C. They noted a dependence of the pseudo-first order reaction rate constant on soot conversion ( $X_{soot}$ ); at low conversion, they observed a maximum in the rate constant from  $0 \leq X_{soot} \leq 25\%$  attributed to rapid destruction of SOFs and other surface functional groups on the soot. This effect was exhibited by different types of soot, such as light and heavy duty vehicle engine soot and graphite spark discharge soot.

Prior research for both thermal catalytic oxidation and PCO of soot has shown that results vary considerably depending on the chemical and physical characteristics of the soot being analyzed. This study develops a reproducible system that will deposit soot on top of a photocatalyst  $TiO_2$  layer and allow reliable determination of PCO soot kinetics. We demonstrate the utility of our technique via alteration of process variables such as soot and  $TiO_2$  loadings to determine their effects on reaction rate, and further test the applicability of our soot series/parallel reaction network and rate

model. More broadly, this study relates to the removal of thick deposits of chemically stable matter intentionally or accidentally coated on photocatalytic self-cleaning materials.

## 2. Experimental setup

### 2.1. $TiO_2$ deposition

Titanium dioxide sol–gel solutions were synthesized using “method 2” of Xu and Anderson [24]. In brief, 16.5 mL titanium isopropoxide (TTIP, Sigma–Aldrich) was added to 200 mL of 0.71 vol% nitric acid ( $HNO_3$ , Fisher Scientific) in deionized (DI, Millipore Milli-Q) water. The TTIP suspension was peptized at room temperature for 3 days. The resultant  $TiO_2$  sol was dialyzed in a SPECTRA/POR molecular porous membrane (Spectrum Laboratories, Inc.) until a final pH value of 3.5 was achieved.

The final  $TiO_2$  sol was deposited on polished quartz crystals and silicon substrates using a spin coater (Headway Research, Inc. PWM32-PS-R790 spinner system) set at 1000 rpm, with a 500 rps ramp rate and a 500 s termination step. The number of  $TiO_2$  spin coats varied from 0 to 8, with a firing step of 100 °C for 1 h between each coat. After all  $TiO_2$  spin coats were deposited on each QCM crystal, the sample was calcined at 350 °C for 3 h with a ramp up rate of 3 °C/min, then cooled to room temperature over 4 h at an approximate rate of 5 °C/min. A Jelight Company Inc. Model #42 ultraviolet-ozone (UVO) cleaner was used to remove any initial organic contaminants on the QCM crystal surface prior to  $TiO_2$  deposition.

### 2.2. Lamp soot deposition

Soot was generated by a hurricane lamp (Ultra-Pure Oil Lamp with 99% Ultra-Pure Paraffin Candle and Lamp Liquid, Lamplight Farms) with a 1.8 cm linear flame, as depicted in Fig. 1. A modulated speed rotator (MSR)/controller (AFMSRX analytical rotator, Pine Instrument Company) was used to deposit this soot on the QCM crystal in a controlled fashion. A smooth alligator clip ( $1\frac{1}{8}$  in. smooth test clips, copper, Radioshack) was attached to the MSR to fasten the QCM crystal to the device. The rotation speed

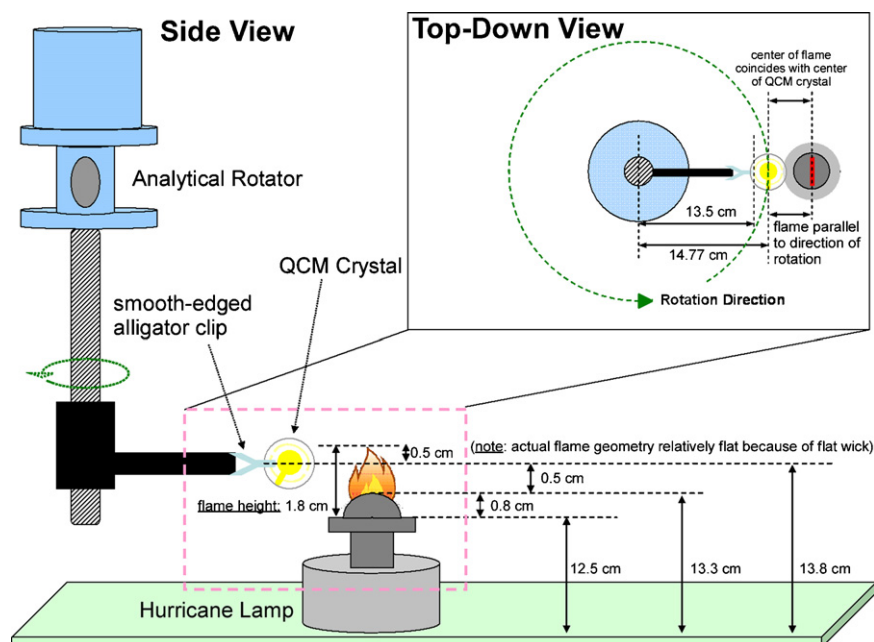


Fig. 1. Schematic of the controlled soot deposition method using an analytical rotator to pass through a hurricane lamp flame.

varied from 5 to 10 rpm ( $\vec{v} = 7\text{--}15\text{ cm/s}$ ;  $\dot{\omega} = 27\text{--}56^\circ/\text{s}$ ), and the QCM crystal passed 0.2–0.5 cm below the top of the undisturbed hurricane lamp flame. For our experiments, the analytical rotor ran at 10 rpm and 0.5 cm into the flame.

### 2.3. Characterization of $\text{TiO}_2$ sol and lamp soot

Following  $350^\circ\text{C}$  calcination,  $\text{TiO}_2$  film roughness was determined by AFM (Dimension 3000, Digital Instruments), with imaging performed in tapping mode (drive frequency: 330 kHz) employing a Si cantilever (Veeco Probes). Measurements were done on  $1\text{ }\mu\text{m} \times 1\text{ }\mu\text{m}$  and  $10\text{ }\mu\text{m} \times 10\text{ }\mu\text{m}$  areas under ambient conditions, with 512 samples per image and 0.5 Hz scan rate. The surface root-mean-square roughness ( $R_q$ ) and the maximum height ( $R_{\text{max}}$ ) calculated by AFM software are defined as the standard deviation of the surface height ( $Z$ ) and the largest  $Z$  difference within the image area, respectively.

Titanium crystal structure was determined using XRD (XRG 3000, Inel Inc.) employing  $\text{Co K}\alpha_1$  radiation ( $\lambda = 1.7890\text{ \AA}$ ). Data was collected using a CPS-120 detector over  $0^\circ < 2\theta < 125^\circ$ , and converted to  $\text{Cu K}\alpha_1$  radiation ( $\lambda = 1.5405\text{ \AA}$ ) with a range of  $0^\circ < 2\theta < 100^\circ$ . The data was calibrated with respect to a silicon standard.

The  $\text{TiO}_2$  film thickness was ascertained by ellipsometry (VASE spectroscopic ellipsometer, J.A. Woollam). The Bruggemann effective medium approximation (BEMA) was employed between 450 and 1100 nm to model the measured  $\psi$  and  $\Delta$  (both in degrees), Stokes parameters related to the polarization change of light interacting with a sample, and correlated to the ratio of complex Fresnel reflection coefficients. For the BEMA, the film was modeled as a two-component mixture of solid  $\text{TiO}_2$  and void volume, where the latter material fraction was fitted. Interfacial roughness/inhomogeneity was added as an additional fitted parameter to capture peak broadening. For  $\text{TiO}_2$  film thickness determinations, ellipsometry measurements were completed for  $\text{TiO}_2$  sol deposited on Si wafers (polished, 500–550  $\mu\text{m}$  thick, Silicon Wafer Microelectronics, Inc.).

To calculate the calcined  $\text{TiO}_2$  film band gap for an allowed direct transition ( $E_{\text{BG,d}}$ ), a generalized oscillator model consisting of 3 Tauc-Lorentz models and 1 Gaussian model was used to fit the refractive index ( $n$ ) and extinction coefficient ( $k$ ) as a function of wavelength ( $\lambda$ ). We were unable to use the BEMA model to determine  $E_{\text{BG,d}}$  because the two-component mixture only modeled  $k(\lambda)$  for  $\lambda > 400\text{ nm}$ . The direct band gap equation is shown in Eq. (1) [25], where  $h$  is Planck's constant ( $6.63 \times 10^{-34}\text{ J s}$ ),  $\nu$  is the frequency ( $\text{s}^{-1}$ ), and  $\alpha$  is the absorption coefficient, where  $\alpha = 4\pi k/\lambda$ .

$$h\nu = E_{\text{BG,d}} + (\alpha h\nu)^2 \quad (1)$$

Soot and  $\text{TiO}_2$  absorption spectra were measured by UV–visible spectrometer (Jasco V-550) in the  $\lambda$  range of 300–800 nm. Visual imaging of soot oxidation was recorded using a Canon Powershot S30 3.2 megapixel digital camera.

### 2.4. Quartz crystal microbalance—theory and application

The quartz crystal microbalance (QCM) is a frequency sensitive technique used to monitor mass changes in our surface studies. The primary component to QCM is its thin quartz crystal plate, with a thinner metal electrode attached to each side of the plate. The electrode material is often gold (Au), but other metals (e.g., Ti, Zn, Pt, Ni, Si, C) can be used. When an electrode is subjected to an alternating electric

field, the quartz crystal vibrates at its resonance frequency, which is sensitive to these properties on the electrode surface: (a) mass changes; (b) mechanical stresses and damping from the density and viscosity of the adjacent fluid; (c) other environmental influences, such as temperature and pressure [26]; and (d) surface roughness of the QCM crystal. The total frequency change ( $\Delta f$ ), Eq. (2), is equal to the sum of the frequency changes caused by each of the five influences described above [27–29], where subscripts  $m$ ,  $T$ ,  $P$ ,  $\eta$ , and  $r$  represent mass, temperature, pressure, viscosity, and roughness, respectively, and  $f_q$  is the fundamental quartz crystal resonance frequency. All  $f$  values are reported in Hz.

$$\Delta f = f - f_q = \Delta f_m + \Delta f_T + \Delta f_P + \Delta f_\eta + \Delta f_r \quad (2)$$

$$\Delta f_m = \frac{-2n f_q^2}{(\mu_q \rho_q)^{1/2}} \Delta m_f = (-n C_q) \Delta m_f \quad (3)$$

The Sauerbrey equation, Eq. (3), relates the QCM frequency shift to the change in mass adsorbed on the quartz crystal surface [30]. Eq. (3) strictly holds for a uniform, rigid, thin film deposit, where  $\Delta f_m$  is the frequency change related to mass,  $n$  is the number of quartz plate sides with adsorbed mass,  $\Delta m_f$  is the mass change per unit area ( $\text{g/cm}^2$ ),  $\mu_q$  is the quartz shear modulus ( $2.947 \times 10^{11}\text{ g/cm s}^2$ ),  $\rho_q$  is the quartz density ( $2.648\text{ g/cm}^3$ ), and  $C_q$  is a constant based on the type of quartz crystal ( $\text{Hz/ng cm}^2$ ). This constant is roughly 0.0566 and 0.0815  $\text{Hz/(ng cm}^2)$  for 5 and 6 MHz QCM crystals at  $20^\circ\text{C}$ , respectively. The Sauerbrey equation is valid (a) for mass loadings less than 2% of the mass/frequency of the bare QCM crystal [31] and (b) when the coated film elasticity has a negligible effect on the QCM crystal's resonance resistance compared to the effect of fluid viscosity on the coated film [32]. Calculations (not shown) prove that both assumptions are valid for our system.

Quartz crystal frequency variations may also be caused by changes in its surrounding fluid, for example, of density, viscosity, pressure, and temperature. The influence of density and viscosity on frequency ( $\Delta f_\eta$ ) were derived by Kanazawa and Gordon [33] for Newtonian fluids, but their effects are negligible in our air–solid system. Frequency increases linearly [29] or parabolically [31] with pressure ( $\Delta f_P$ ), but we neglect this influence because we run an isobaric system operating at near standard pressure. We also ignore QCM crystal roughness ( $\Delta f_r$ ) because polished crystals are used in our system. Average electrode surface roughness is 5 nm for polished crystals versus 1800 nm for unpolished crystals according to the QCM crystal manufacturer.

The temperature impact on frequency for AT-cut ( $35^\circ 15'$  with respect to the crystal axes [34]) crystals is shown below in Eq. (4), where  $\Delta f_T$  is the frequency change related to temperature,  $T$  is the temperature ( $^\circ\text{C}$ ) and  $a_0$ – $a_3$  are empirical temperature coefficients [27,35]. Experimental data from the QCM manufacturer fitted to Eq. (4) yielded a  $-0.5\text{ Hz} < \Delta f_T < 0.5\text{ Hz}$  shift for 20 and  $40^\circ\text{C}$ , respectively, which is negligible compared to our observed  $\Delta f$  values of greater than 100 Hz.

$$\Delta f_T = a_3 T^3 + a_2 T^2 + a_1 T + a_0 \quad (4)$$

Our QCM phase lock oscillators (PLO), crystal holders, and 1 in. diameter crystals (5 MHz crystals, Au electrode, part #149257-1; 6 MHz crystals, Pt electrode, part #149281-1) were purchased from Inficon (formerly Maxtek, Inc.). All crystals are AT-cut and optimized for  $25^\circ\text{C}$  operating temperature.

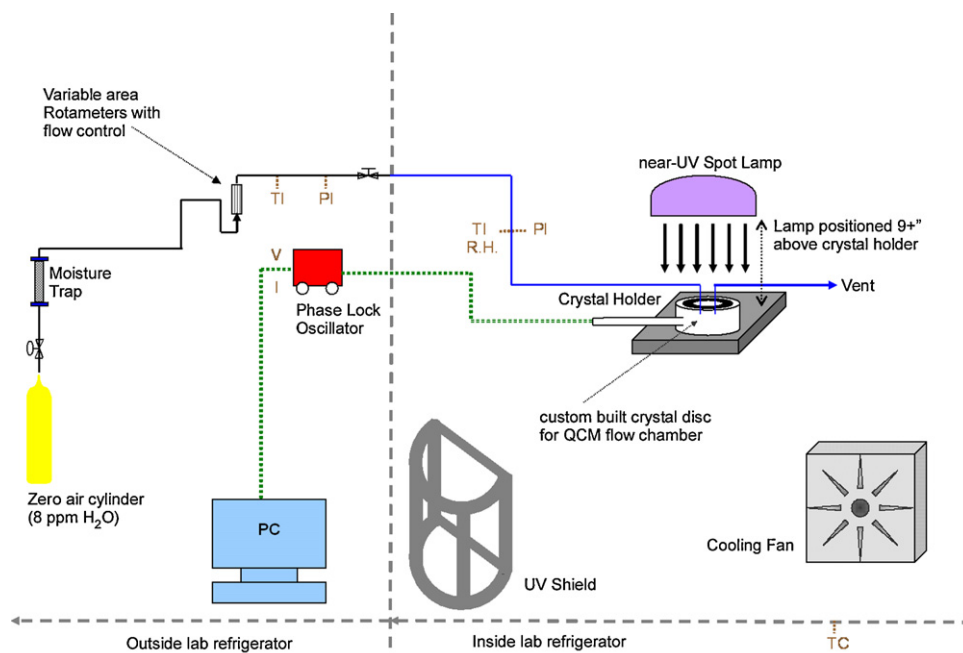


Fig. 2. Process flow schematic of the quartz crystal microbalance reaction experiments.

### 2.5. Experimental reaction setup

Fig. 2 is a process flow schematic of the reaction experiments. Zero air (8 ppm  $\text{H}_2\text{O}$ , 1 ppm THC) flows through a moisture trap and is piped into a refrigerator (model 3927 incubator, Forma Scientific) containing the QCM crystal holder. A variable area rotameter (K-03216-12 flowmeter, Cole Parmer) controls the volumetric zero-air flow rate at 55 mL/min. A quartz flow chamber was manufactured to enclose and shield the QCM crystal from exposure to laboratory air and to create a controlled atmosphere surrounding the crystal. The  $1\frac{5}{16}$  in. diameter,  $1/16$  in. thick quartz discs (Prism Research Company, Raleigh, NC) contained two  $1/16$  in. holes drilled through the disc. Two  $1/16$  in. OD stainless steel pipes (Swagelok) are inserted into the holes to allow zero-air flow into and out of the chamber.

A spot lamp (100 W Black-Ray B-100A, UVP, LLC) positioned 9+ in. above the crystal holder emits UVA light ( $300 < \lambda < 400$  nm,  $\lambda_{\text{max}} = 365$  nm). A cooling fan helped maintain the refrigerator cavity at uniform temperature, and a UV shield (Safety Shield 6350, Nalgene) in front of the UV spot lamps protects the user. Vibration dampening pads are positioned below the crystal holders to prevent any external vibrations from causing a frequency shift.

Soot PCO occurs within the UV-illuminated flow chamber and the effluent gas (zero-air feed plus oxidation products, presumably  $\text{CO}_2$  and  $\text{H}_2\text{O}$ ) is vented into the refrigerator cavity. The QCM PLOs are interfaced with a controller and data acquisition software (NI SC-2345 signal conditioning connector box and LabView version 8.20, respectively, National Instruments) for data collection of crystal frequency and voltage (53131A 225 MHz universal counter and 34401A 6  $1/2$  digital multimeter, respectively, Agilent Technologies), and refrigeration temperature (K thermocouple, Omega Engineering). The zero-air flow temperature and relative humidity (R.H.) are measured using a thermohygrometer (Traceable memory hygrometer/thermometer model 4185, Control Company) interfaced with a computer using data acquisition software (Control Company). A pressure transducer (Omega Engineering) measures the air pressure. All experiments are run between  $28^\circ\text{C} \pm 2.5^\circ\text{C}$  and 0 psig, with trace  $\text{H}_2\text{O}$  in the air flow.

### 2.6. Data analysis and kinetic modeling

The mixed series/parallel network model for soot photooxidation we proposed previously [9] for predicting both mass loss and  $\text{CO}_2$  generation is reproduced in Fig. 3. The resulting kinetic model (Eqs. (5a), (5b), (6)) [9] is the “simple” model we previously employed for the photocatalyzed soot single experiment mass loss data of Lee and Choi [6]. These equations (Eq. (5a), (5b)) describe the mass rate change in adherent soot and adsorbed intermediate(s), where  $m_{\text{soot}}$  and  $m_{\text{int}}$  are the soot and intermediate masses (ng), respectively. These equations are solved analytically to give the change in soot and intermediate masses as a function of time, where the rate constants  $k_1$ ,  $k_2$ , and  $k_3$  ( $\text{min}^{-1}$ ) are functions of incident UV light intensity arriving at the  $\text{TiO}_2$  top surface. The fractional remaining mass is the dimensionless  $m(t)/m_0$ , with solution given in Eq. (6).

$$\frac{dm_{\text{soot}}}{dt} = -k_1 m_{\text{soot}} - k_2 m_{\text{soot}} = -(k_1 + k_2) m_{\text{soot}} \quad (5a)$$

$$\frac{dm_{\text{int}}}{dt} = k_2 m_{\text{soot}} - k_3 m_{\text{int}} \quad (5b)$$

$$\begin{aligned} \frac{m}{m_0} &\approx \frac{m_{\text{soot}} + m_{\text{int}}}{m_{\text{soot},0}} \\ &= \exp[-(k_1 + k_2)t] + \frac{k_2}{k_3 - (k_1 + k_2)} \{ \exp[-(k_1 + k_2)t] \\ &\quad - \exp(-k_3 t) \} \end{aligned} \quad (6)$$

Since soot deposited above the  $\text{TiO}_2$  thin film will absorb some UV light, the rate constants are corrected for UV absorbance by the

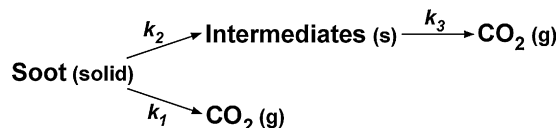


Fig. 3. A series/parallel reaction mechanism to describe soot photooxidation by  $\text{TiO}_2$ .



soot layer (Eq. (7)), and the intensity  $I_0$  refers to that incident on top of the soot layer.

$$k_i = k_{0,i} I^p = k_{0,i} \{I_0 \exp[-\varepsilon_{\text{soot}} \delta_{\text{soot}}(t)]\}^p \quad (7)$$

where  $i = 1, 2, 3$  and  $0.5 \leq p \leq 1.0$

The soot thickness,  $\delta_{\text{soot}}(t)$  ( $\mu\text{m}$ ), is related to the residual mass via Eq. (8).

$$\delta_{\text{soot}}(t) \approx \delta_{\text{soot}}(0) \left[ \frac{m(t)}{m_0} \right] \quad \text{where } m(t) = m_{\text{soot}}(t) + m_{\text{int}}(t) \quad (8)$$

This model has two fixed parameters: (a) the initial soot thickness  $\delta_{\text{soot}}(0)$ , and (b) the exponent for rate constant dependence on light intensity,  $p$ . We choose  $p = 1$ , but previous work [9] shows relative insensitivity to different values from  $0.5 \leq p \leq 1$ . Additionally, there are four fitted parameters: the intensity-independent kinetic rate constants  $k_{0,1}$ ,  $k_{0,2}$ ,  $k_{0,3}$  ( $\text{cm}^2/\text{mW min}$ ), and the apparent UV absorption coefficient of soot,  $\varepsilon_{\text{soot}}$  ( $\mu\text{m}^{-1}$ ). Mathematical analyses for model fitting were completed using the Solver function in Excel<sup>®</sup> (Microsoft), Origin (OriginLab), or Matlab (The Mathworks, Inc.).

### 3. Results and discussion

#### 3.1. Atomic force microscopy (AFM)

A QCM crystal with four spin coats of  $\text{TiO}_2$  sol calcined at  $350^\circ\text{C}$  is studied using AFM. The surface height root-mean-square for a  $10 \mu\text{m} \times 10 \mu\text{m}$  area is  $3.7 \text{ nm}$ , which reflects an overall standard deviation in height differential of less than 5% of total  $\text{TiO}_2$  thickness. The surface roughness for our  $\text{TiO}_2$ -coated samples is low; i.e., the calcined film is a nearly non-porous, continuous layer.

#### 3.2. X-ray diffraction (XRD)

The XRD result for the Au electrode QCM crystal with four spin coats of  $\text{TiO}_2$  sol calcined at  $350^\circ\text{C}$  is shown in Fig. 4. Minor differences between the XRD peaks and the powder diffraction file data [36] are caused by Si calibration shifts. The most intense diffraction peak belongs to the quartz crystal ( $2\theta = 26.8^\circ$ ), while the four next largest peaks are identified with the Au electrode. Three peaks ( $2\theta = 25.0^\circ$ ,  $37.8^\circ$ ,  $53.9^\circ$ ) are recognized as anatase phase  $\text{TiO}_2$ , while a shoulder peak ( $2\theta = 28.0^\circ$ ) may be related to rutile

phase  $\text{TiO}_2$ . Therefore, we assume a predominately anatase phase  $\text{TiO}_2$  crystallinity for our calcined sol, as expected for sol-gel derived  $\text{TiO}_2$  calcined at temperatures from  $350$  to  $500^\circ\text{C}$  [37–42]. Specifically, Fu et al. [42] detected 90% anatase/10% rutile structure and  $71 \text{ \AA}$   $\text{TiO}_2$  crystallite size using a similar sol-gel preparation technique (dialysis pH 4, calcination temperature =  $300^\circ\text{C}$ , pelletized  $\text{TiO}_2$ ). For calcination above  $500^\circ\text{C}$ , the resultant predominant phase is rutile [42].

#### 3.3. Spectroscopic ellipsometry (SE)

To determine  $\text{TiO}_2$  film thickness, SE was used to model the optical parameters  $n$  (refractive index) and  $k$  (extinction coefficient). The original model assumed a single-component  $\text{TiO}_2$  material, which yielded a poor fit to  $\Psi$  and  $\Delta$ . We then used the BEMA two-component model of  $\text{TiO}_2$  and void volume, which captured well the peaks for  $\Psi$  and  $\Delta$  as a function of  $\lambda$ . In addition, surface inhomogeneity was added as an additional parameter to account for peak broadening. Fig. 5a shows the results of  $\text{TiO}_2$  film thickness as a function of the number of  $\text{TiO}_2$  spin coats on Si wafers. Overall, the mean square error ranged from 1 to 3, with

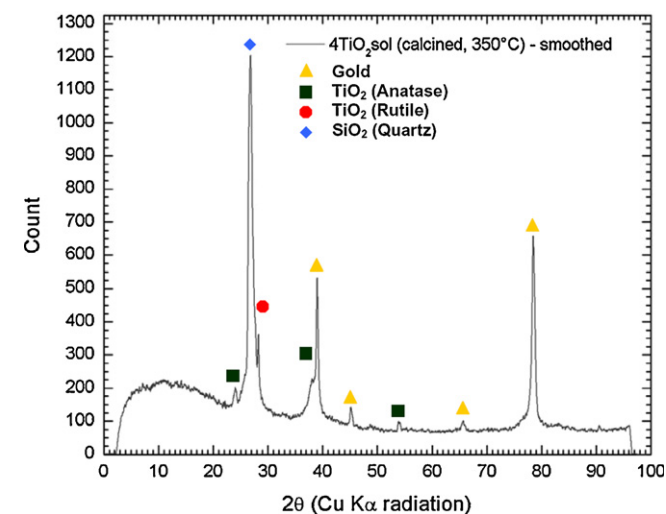
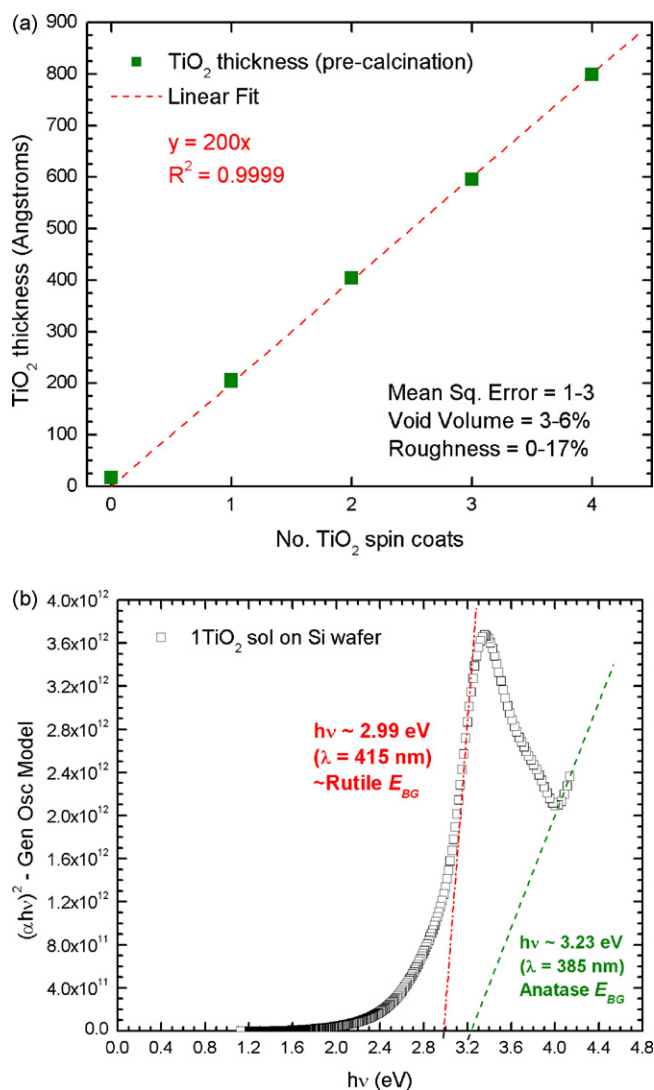


Fig. 4. Smoothed XRD image of a QCM crystal with four spin coats of  $\text{TiO}_2$  sol, calcined at  $350^\circ\text{C}$ . The symbols represent different crystal structures.

Fig. 5. Spectroscopic ellipsometry results of  $\text{TiO}_2$  sol spin coated on Si wafers: (a)  $\text{TiO}_2$  thickness as a function of the number of spin coats; (b) optical absorption spectrum for the  $\text{TiO}_2$  thin film calcined at  $350^\circ\text{C}$ , graphed as  $(\alpha h\nu)^2$  as a function of photon energy ( $h\nu$ ) for direct band gap transitions.

void volumes of 3–6% and surface roughness of 0–17%. The higher the number of spin coats, the higher the void volume and surface roughness. A simple linear fit captures the data well, thus each resulting spin coat deposited 20 nm (200 Å) of TiO<sub>2</sub> film on the Si wafer. This test shows that we can deposit a reproducible amount of TiO<sub>2</sub> on a substrate using a spin coater. Similar SE measurements of TiO<sub>2</sub> films equivalently deposited on QCM crystals as the substrate yielded poor model fits to  $\psi$  and  $\Delta$ . This latter result occurs because the Au electrode absorbs light significantly in the wavelength range studied, an effect not included in the model. Nonetheless, we may assume that our TiO<sub>2</sub> layers deposited on the QCM varied linearly with the number of spin coats, as shown for Si wafers (Fig. 5a).

Additionally, we can use SE to determine the band gap energy  $E_{\text{BG,d}}$  for the TiO<sub>2</sub> film on Si. A generalized oscillator model was used to determine  $k(\lambda)$  for the calcined, TiO<sub>2</sub>-coated Si wafer. Fig. 5b shows the optical absorption spectrum (Eq. (1)), graphed as  $(\alpha h\nu)^2$  for direct transitions, as a function of photon energy ( $h\nu$ ). The shape of the data allows for two direct band gap transitions. Fitting a linear curve to the steepest data, we estimate two  $E_{\text{BG,d}}$  of 2.99 eV ( $\lambda \sim 415$  nm) and 3.23 eV ( $\lambda \sim 385$  nm). These  $E_{\text{BG,d}}$  correlate well to the bulk band gaps of rutile phase (3.05 eV or  $\lambda \sim 407$  nm) and anatase phase (3.26 eV or  $\lambda \sim 380$  nm) TiO<sub>2</sub> crystallinity [43], respectively. The dual crystal structure arising from the band gap transitions corresponds nicely with the XRD results.

### 3.4. UV–vis spectroscopy

We used UV–vis spectroscopy to determine the soot layer absorption ( $\lambda = 350$  nm) as a function of the number of deposition passes through the hurricane lamp (Fig. 6a). The UV spectra were done with no TiO<sub>2</sub> layer. These results show that we can linearly and reproducibly deposit soot using a hurricane lamp. We can control the amount of soot deposited on the QCM crystal by varying any of four parameters: (a) the number of passes through the hurricane lamp; (b) the speed of the analytical rotor; (c) the flame height; and (d) sample position in the flame. For photocatalyzed sample preparation, we choose a 10 rpm rotor speed and a sample distance of 0.5 cm into the flame because we obtain a range from approximately 50% to 1% UV transmission ( $\lambda = 350$  nm) through the soot layer when we prepare samples by one, two, four, and eight passes through the lamp flame (Fig. 6a).

Quartz glass slides were coated with four and eight spin coats of TiO<sub>2</sub> sol, then were calcined at 350 °C for 1 h, the same procedure as for the QCM crystals. The UV–vis spectroscopy results (Fig. 6b) show that for  $\lambda > 400$  nm, the absorption spectra are comparable for both TiO<sub>2</sub> coatings. If we weight the Abs values from 300 nm  $< \lambda < 400$  nm (the spectral range of the UV bulb) using a Gaussian distribution ( $A = 40.89$ ,  $\sigma = 33.32$ ,  $\mu = 350$ ) for the  $I(\lambda)$  emission of the UV lamp, the average integrated Abs is 0.04 and 0.08 for four and eight TiO<sub>2</sub> layers, respectively. For our structured TiO<sub>2</sub>, double the thickness yields twice the amount of UV light absorbed.

### 3.5. Soot photooxidation—effect of single and multiple soot layers

Soot oxidation was investigated using samples prepared by one, two, four and eight passes of deposited soot. The TiO<sub>2</sub> loading was kept constant at 4 spin coats, or 80 nm thickness. Fig. 7 shows the visual change in the QCM crystal for the different deposition steps, as well as after TiO<sub>2</sub> soot oxidation. Fig. 7a is a photo of a bare QCM crystal, while Fig. 7b shows a TiO<sub>2</sub>-coated QCM crystal. Fig. 7c depicts a sample for a single pass of soot deposited on the TiO<sub>2</sub>-covered QCM crystal. Fig. 7d represents soot photooxidation after

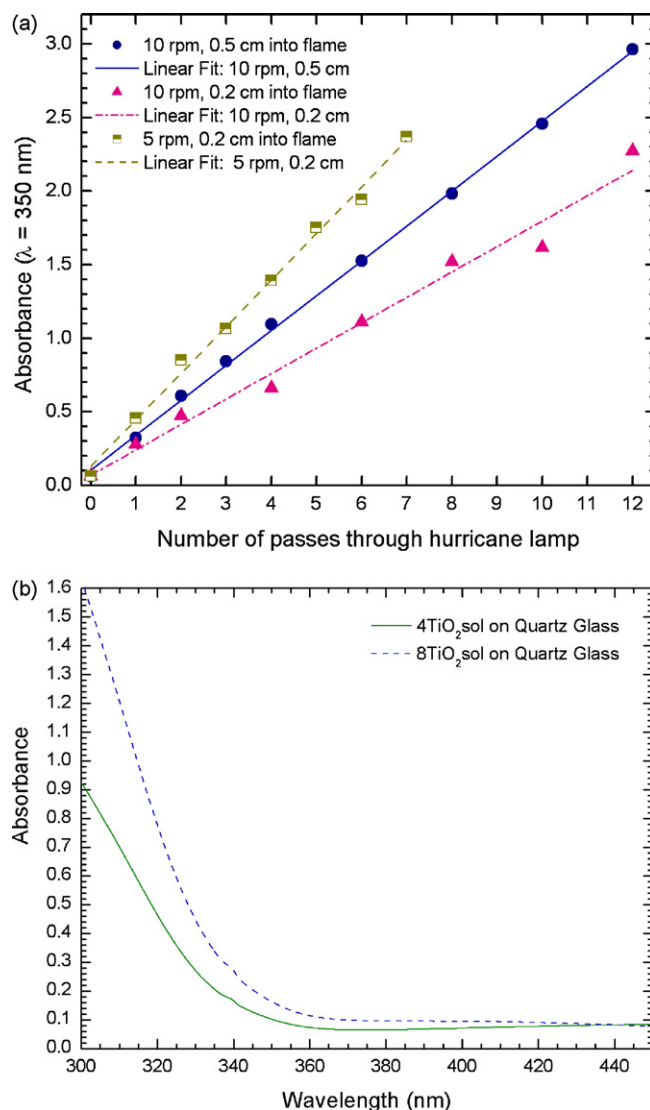


**Fig. 6.** UV–vis spectroscopy results on quartz glass for (a) soot absorption ( $\lambda = 350$  nm) as a function of the number of passes through hurricane lamp flame for different analytical rotor speeds and distance from the top of the flame; (b) TiO<sub>2</sub> absorption for four and eight spin coats of TiO<sub>2</sub> sol.

11,000 min of UV illumination, and shows an image very similar to Fig. 7b, corresponding to a soot-free TiO<sub>2</sub> surface.

The change in soot mass as a function of time for the four different soot loadings appears in Fig. 8a. Several experiments were duplicated to check reproducibility. For the single and double passes through the hurricane lamp, the mass change  $\Delta m$  ultimately levels off at longer time, indicating complete soot oxidation. In each case, the final frequency value was similar to the frequency of the soot-free crystal, providing independent verification of the mass balance for total soot photooxidation. The one pass  $\Delta m$  (total) is about 3000 ng, and the two pass result is 6200 ng, showing consistent deposition rates for these two samples.

For the four pass sample, photooxidation is incomplete after 14,000 min ( $\sim 10$  days) of UV illumination. From the Sauerbrey equation, we estimate 55% soot oxidation of this sample at run termination.

For eight passes through the hurricane lamp, the soot film is visibly opaque. The  $\Delta m$  initially decreases with UV illumination time, and then shows a slow, steady increase from 1000 to

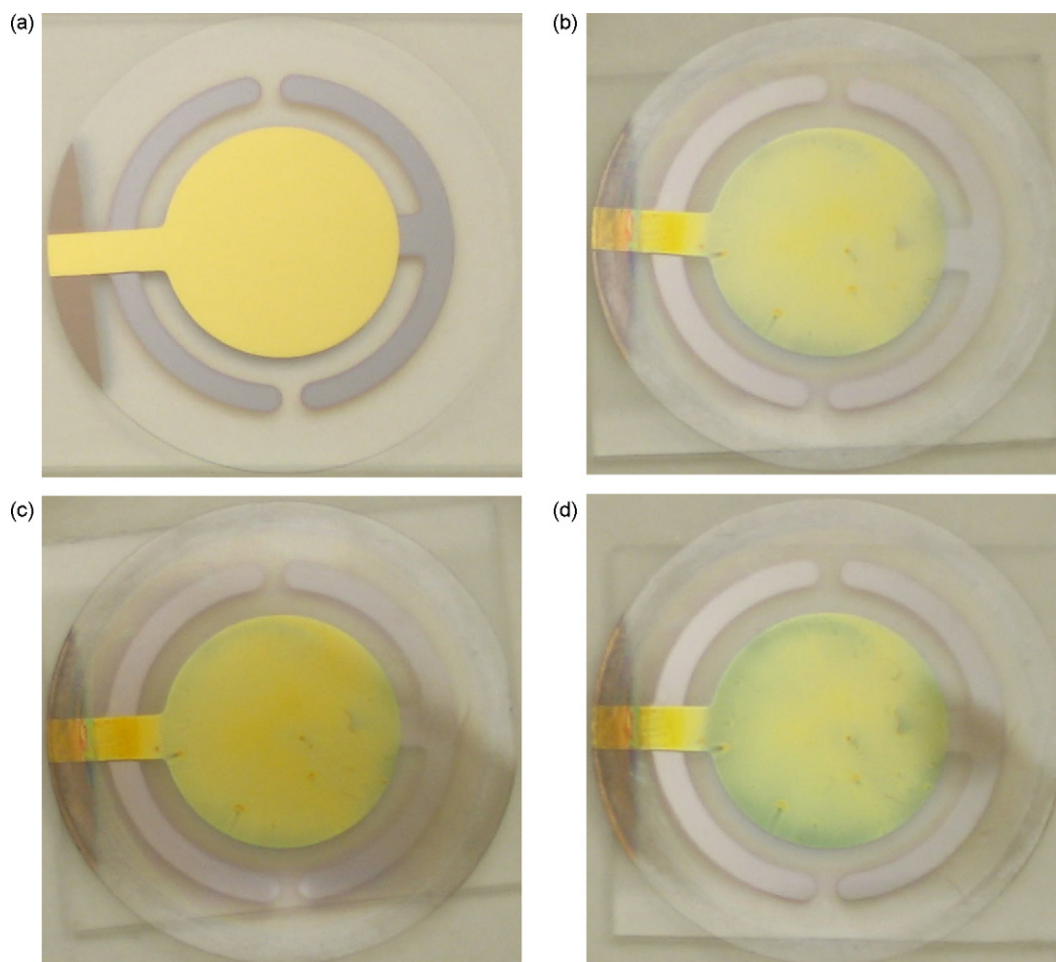


**Fig. 7.** Visual results of soot oxidation for a QCM crystal spin coated four times with  $\text{TiO}_2$  sol, then deposited with a single pass of hurricane lamp soot: (a) bare crystal; (b)  $\text{TiO}_2$ -coated crystal (pre-soot deposition); and soot/ $\text{TiO}_2$ /crystal after (c) 0 min; and (d) 11,000 min of UV illumination time.

15,000 min before leveling off. From Fig. 6a, eight passes through the hurricane lamp yields a soot absorbance ( $\lambda = 350$  nm) of 1.98, or 1% UV transmission. Therefore, minimal soot PCO occurs because the soot screens nearly all UV light incident to the  $\text{TiO}_2$  layer. There appears to be two distinct regions to this data: (a) initial rapid desorption, followed by (b) slow adsorption and/or non-catalyzed photooxidation. The short, fast desorption phase is from 0 to 700 min, where presumably any volatile organic material leaves the soot surface. The subsequent adsorption/oxidation phase lasts from 1000 to 15,000 min, as indicated by a steady increase in mass on the QCM crystal. The data in this region can be fit by a simple linear equation:  $\Delta m = 0.0604t - 483.69$ .

We propose two explanations for the adsorption/oxidation phase. First, trace  $\text{H}_2\text{O}$  from the feed air stream can adsorb on the soot, causing the observed mass increase rate of 0.0604 ng/min. This value translates to 0.0384 ppmv of  $\text{H}_2\text{O}$  in the flowing air of 55 mL/min, which is within reasonable limits for trace  $\text{H}_2\text{O}$  in the feed air, even after passing through the moisture trap. (We expect a minimum of 0.4 ppmv in the air stream according to our in-line thermohygrometer measurements. This value is a rough approximation because it is below the specified detection limits – 10–95% R.H., greater than  $\pm 4\%$  error for R.H. < 10% – of the thermohygrometer.) Previous researchers have detected water adsorption on oxygenated surface sites for soot [44–47] and activated carbon [48,49].

Second, the soot may experience non-catalyzed, homogeneous photooxidation to create additional oxygenated organic function-

alities and/or compounds on the soot surface. Photons in the near-UV range have energies ranging from 300 to 400 kJ/mol, which are sufficient to cause C–C and C–H bond dissociations to form free radicals [50]. The radicals should quickly react with nearby molecular oxygen, and eventually can form carboxylic and carbonyl groups. For example, it is common to see sunlight photooxidation of plastics (e.g., polystyrene, polyethylene terephthalate), causing a discoloration [50] or a “yellowing” effect.

For UV-illumination times after 15,000 min,  $\Delta m$  levels off at 350 ng. In any event, these effects would not change the ultimate  $\Delta m$  values of one and two pass soot experiments because no soot remained as  $t$  approached 20,000 min. It may make a modest contribution to the  $m(t)$  curve shape, which we have not included in our modeling.

### 3.6. Soot photooxidation—effect of $\text{TiO}_2$ thickness

We next altered the number of  $\text{TiO}_2$  sol spin coats from zero to eight coating layers, and held soot deposition to one pass through the lamp flame. The  $\text{TiO}_2$  thickness was 0, 80, and 160 nm, for zero, four, and eight coats, respectively (Fig. 5a).

Fig. 8b shows the change in soot mass as a function of time for the different  $\text{TiO}_2$  loadings. For the “blank” experiment with no  $\text{TiO}_2$  layer, an initial mass change of  $-50$  ng corresponds again to thermal desorption and/or photooxidation on the soot surface. After a short flat period to 2000 min, a monotonic increase in the



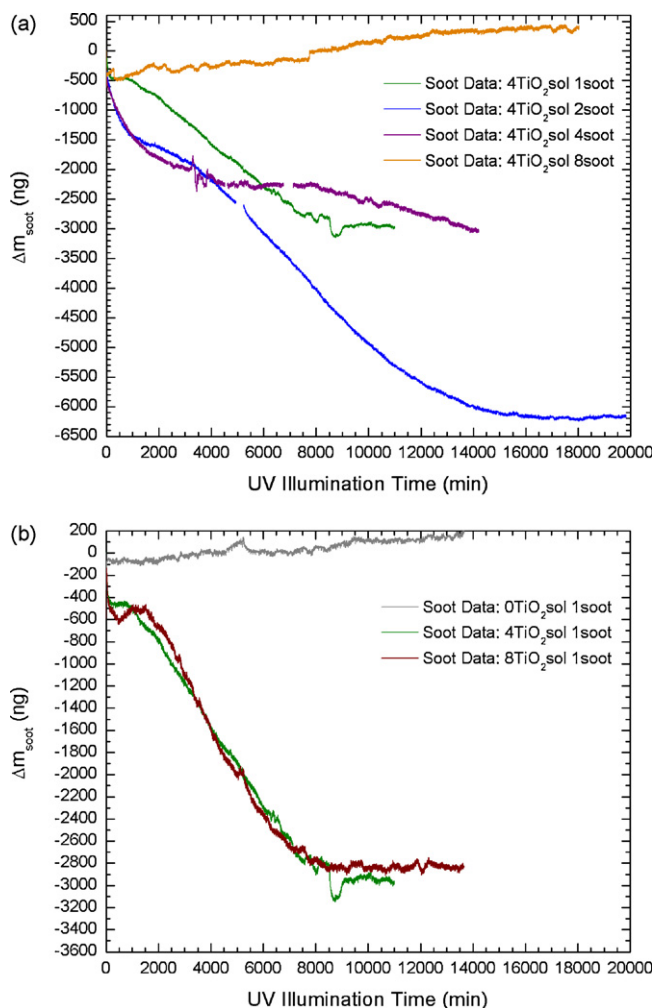


**Fig. 8.** Soot photocatalyzed oxidation as a function of time for QCM crystals deposited with TiO<sub>2</sub>, then soot: (a) four spin coats of TiO<sub>2</sub> sol, and one, two, four, and eight passes of soot using the analytical rotor; (b) zero ("blank"), four, and eight spin coats of TiO<sub>2</sub> sol, and a single pass through the lamp flame.

mass change to 150 ng at 13,000 min is seen. Similar to the previous data with eight passes through the lamp flame, we assume H<sub>2</sub>O adsorption on and/or homogeneous photooxidation of the soot layer. The "blank" experiment data suggests minimal  $\Delta m$  shift caused by the near-UV light for single soot pass, so we do not include this contribution in our modeling.

The data for four and eight coats of TiO<sub>2</sub> sol show nearly identical soot loadings and soot oxidation rates. We expect the eight coat TiO<sub>2</sub> sol to react soot faster than the four coats of TiO<sub>2</sub> sol; results from Fig. 6b and the analysis above reveal that in the spectral range of the UV bulb the 8TiO<sub>2</sub> sol coating absorbs double the amount of UV light than the 4TiO<sub>2</sub> sol coating.

While the four and eight spin coats of TiO<sub>2</sub> exhibit different TiO<sub>2</sub> thicknesses, the surface area in direct contact with soot may not vary significantly between the two samples if there is virtually no penetration of soot into the TiO<sub>2</sub> layers. Research on the direct, lateral, and remote oxidation of organics by TiO<sub>2</sub> show a dominant reaction rate for direct oxidation compared to lateral or remote oxidation mechanisms [6,8,51,52] which require surface or gas phase transport of oxidants. Lee et al. [8] deposited 0.5  $\mu\text{m}$  thick candle soot on TiO<sub>2</sub> and TiO<sub>2</sub>-free films and observed complete destruction of soot in direct contact with the TiO<sub>2</sub> film in 4.5 h. Lateral oxidation of their soot film required 155 h, or a 35 $\times$  increase in reaction time versus direct oxidation, and remote

oxidation of a similar soot film 175  $\mu\text{m}$  from the TiO<sub>2</sub> layer needed 305 h, or 70 $\times$  longer compared to direct oxidation. Lee and Choi [6] monitored the oxidation of *n*-hexane soot on TiO<sub>2</sub> and claimed that direct oxidation of soot must occur first, prior to lateral soot oxidation. Haick and Paz [52] observed fast ( $t < 20$  min) degradation of octadecyltrichlorosilane (OTS) coated on TiO<sub>2</sub> when UV light is exposed to TiO<sub>2</sub>, attributed to direct oxidation. Slower OTS degradation rates at longer times ( $t = 240$ –1000 min) were required for lateral oxidation of OTS adjacent to a UV-illuminated TiO<sub>2</sub> surface. Kubo et al. [51] calculated the quantum yield of H<sub>2</sub>O<sub>2</sub> production, assumed to be the diffusing species for remote photocatalytic oxidation, as  $1.8 \times 10^{-7}$ , which is considerably lower than, for example, direct oxidation of soot, calculated as  $1.1 \times 10^{-4}$  by Mills et al. [7].

Therefore, we expect that the soot in contact with the surface TiO<sub>2</sub> layer to exhibit the fastest oxidation and that free radical generation and migration from the bulk TiO<sub>2</sub> to its surface is negligible by comparison. Under this assumption, we do not expect large differences in soot oxidation rate for different TiO<sub>2</sub> thicknesses because of similar soot/TiO<sub>2</sub> contact area for all cases. Our SE results of 3–6% TiO<sub>2</sub> void volume and 0–17% surface roughness confirm that (a) a minimal amount of soot will enter the TiO<sub>2</sub> layer because of its low porosity and (b) there are only minor inhomogeneities in the TiO<sub>2</sub> surface for different thicknesses.

### 3.7. Soot photooxidation—kinetic modeling

The series/parallel reaction mechanism, described in Fig. 3 and Eqs. (5)–(8), was used to model the soot data that exhibited complete photooxidation. Fig. 9 shows model fits for four spin coats of TiO<sub>2</sub> sol and one or two passes through the hurricane lamp. Table 1 reports the results of the four fitted parameters for the soot data modeled. Overall, for each  $k_{0,i}$  and  $\epsilon_{\text{soot},i}$ , the fitted parameter values for each experiment fall within the same order of magnitude. The average relative error between the model and the data ranged from 2 to 5% for  $t > 1000$  min. We neglect the initial 1000 min because of the significant mass loss in this short time, which is not captured in our reaction mechanism. Two phenomena may contribute to this early decrease in  $\Delta m$ .

First, a QCM frequency shift is seen when UV light is shone on the QCM crystal for  $t < 30$  min. Tests on bare and soot-coated QCM crystals (not shown) reveal a frequency change when UV light initially strikes the crystal, shifting  $\Delta m = -300$  ng to  $-650$  ng. We

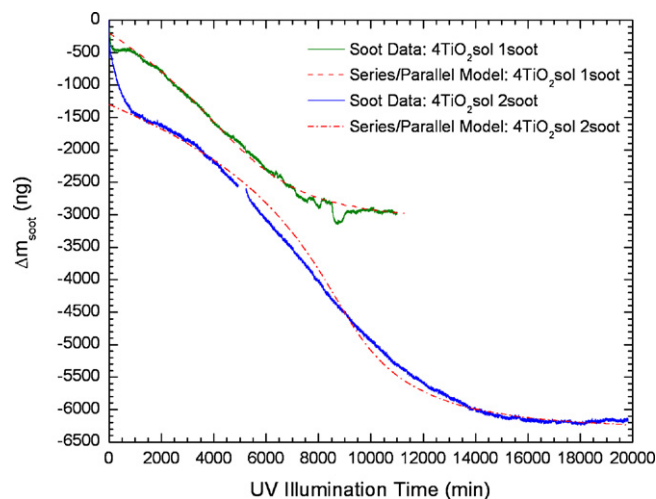


**Fig. 9.** Series/parallel reaction mechanism, described in Fig. 3, for QCM crystals spin coated four times with TiO<sub>2</sub> sol. Model fit to the experimental data for and single and double passes through the lamp flame.



**Table 1**Fitted parameter values for the series/parallel reaction model ( $p = 1$ ).

Experiment data	$k_{0,1}$ cm <sup>2</sup> / (mW min)	$k_{0,2}$ cm <sup>2</sup> / (mW min)	$k_{0,3}$ cm <sup>2</sup> / (mW min)	$\epsilon_{\text{soot}}$ (μm <sup>-1</sup> )
4TiO <sub>2</sub> sol, 1 soot	$5.56 \times 10^{-5}$	$1.66 \times 10^{-6}$	$3.33 \times 10^{-7}$	3.72
4TiO <sub>2</sub> sol, 2 soot	$4.04 \times 10^{-5}$	$9.05 \times 10^{-7}$	$5.33 \times 10^{-7}$	3.00
2TiO <sub>2</sub> sol, 1 soot	$2.74 \times 10^{-5}$	$2.20 \times 10^{-6}$	$5.66 \times 10^{-7}$	3.69
8TiO <sub>2</sub> sol, 1 soot	$7.37 \times 10^{-5}$	$1.99 \times 10^{-6}$	$1.27 \times 10^{-7}$	5.00
Average values	$4.92 \times 10^{-5}$	$1.69 \times 10^{-6}$	$3.90 \times 10^{-7}$	3.85

assume this shift is related to surface thermal desorption; alternating blocking and allowing UV light to reach the crystal did not alter the  $\Delta m$  appreciably after the initial presumed desorption.

Second, the rest of the initial  $\Delta m$  loss (30 min <  $t$  < 1000 min) likely relates to the photolytic oxidation into volatile oxygenates of unburned HCs, SOFs or VOFs in direct contact with the TiO<sub>2</sub>. The organic carbons would deposit directly on the porous soot [12] and may contact most of the TiO<sub>2</sub> surface as well. It is reasonable to believe that the  $\Delta m$  loss in this regime is attributed to HC and SOF/VOF degradation because (a) it is more readily accessible to the TiO<sub>2</sub> and (b) the organic carbons are easier to react than the graphitic carbons in soot. These results parallel the different kinetic reaction rates and regimes seen for the thermal catalytic oxidation of organic and graphitic carbon [13,15,20–22]. Moreover, previous literature on adsorbed organic layers, such as stearic acid [39,53–55], palmitic acid [56], and fluoranthene [57], deposited on TiO<sub>2</sub> thin films has shown burn off times ranging from 250 min to over 700 min. Sitkiewitz and Heller [55] used a 300 nm TiO<sub>2</sub> sol–gel film for the destruction of a 200 nm stearic acid (C<sub>18</sub>H<sub>36</sub>O<sub>2</sub>) layer. They estimated a zero-order kinetic rate constant of 0.21 nmol (–CH<sub>2</sub>–)/[cm<sup>2</sup> min (mW/cm<sup>2</sup>)], assuming 1 mol CO<sub>2</sub> produced per carbon reacted. Romeas et al. [56] similarly observed an apparent zero-order kinetics of 5.3 nmol (–CH<sub>2</sub>–)/[cm<sup>2</sup> min (mW/cm<sup>2</sup>)] for the destruction of a 580 nm thick palmitic acid layer. Over 900 min was needed for complete film mineralization. These reaction times for adsorbed high molecular weight hydrocarbons are comparable to our short time organic carbon PCO data.

### 3.8. Soot photooxidation—model predictions

The series/parallel model can be used to predict the UV illumination time required for soot oxidation using four spin coats of TiO<sub>2</sub> and one, two, four, and eight passes through the lamp flame (Fig. 10). The model predicts complete soot oxidation for a single and double passes of deposited soot. For four passes through the lamp flame, the model predicts only partial soot oxidation of  $\Delta m = -1450$  ng or 13% soot oxidation after 20,000 min of UV illumination. Predicted soot oxidation is negligible for eight passes of deposited soot because it screens nearly all UV light from the TiO<sub>2</sub> top layer, with  $\Delta m = -60$  ng or 0.25% soot oxidation after 20,000 min. Qualitatively, the model predicts trends similar to the actual data: (a) complete soot oxidation of one and two passes of deposited soot; (b) partial soot oxidation for four passes of deposited soot; and (c) negligible soot oxidation for eight passes through the lamp flame.

We can use the reaction rates calculated from the series/parallel model to determine  $\phi$ , the formal quantum efficiency (FQE), defined in Eq. (9). We calculate that 1 mW/cm<sup>2</sup> of near-UV light ( $\lambda = 365$  nm) is 1.8 photons/(cm<sup>2</sup> s) [58]. A full description of the FQE computation is described previously [59]. Table 2 lists the calculated initial FQEs for our soot oxidation data. Two types of FQEs are calculated, one for the light intensity incident on the soot layer ( $r_{\text{soot}}/I_{\text{soot}}$ )<sub>initial</sub> and ( $r_{\text{soot}}/I_{\text{soot}}$ )<sub>max</sub>, where  $I_{\text{soot}} = 1.3 \times 10^{16}$  photons/s, and one incident on the TiO<sub>2</sub> layer corrected for soot

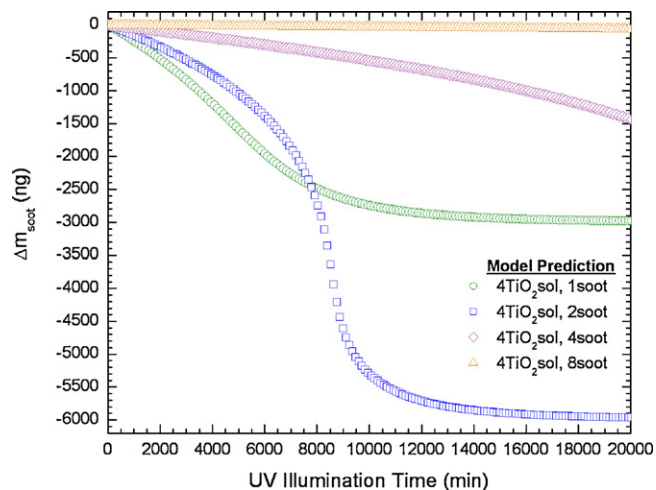


**Fig. 10.** Series/parallel reaction mechanism, described in Fig. 3, for QCM crystals spin coated four times with TiO<sub>2</sub> sol. Model prediction using averaged fitted parameter values (Table 1) for one, two, four, and eight passes through the lamp flame.

**Table 2**

Formal quantum efficiencies for the series/parallel reaction model ( $p = 1$ ), where the incident light intensity is determined at the top of the soot layer ( $r_{\text{soot}}/I_{\text{soot}}$ ) or the top of the TiO<sub>2</sub> layer ( $r_{\text{soot}}/I_{\text{TiO}_2}$ ). Initial ( $t = 0$ ) and maximum FQEs are reported.

Experiment data	Initial FQE ( $r_{\text{soot}}/I_{\text{soot}}$ ) <sub>initial</sub>	Maximum FQE ( $r_{\text{soot}}/I_{\text{soot}}$ ) <sub>max</sub>	Initial and maximum FQE ( $r_{\text{soot}}/I_{\text{TiO}_2}$ )
4TiO <sub>2</sub> sol, 1 soot	$6.26 \times 10^{-4}$	$8.03 \times 10^{-4}$	$3.10 \times 10^{-3}$
4TiO <sub>2</sub> sol, 2 soot	$9.30 \times 10^{-4}$	$9.53 \times 10^{-4}$	$3.95 \times 10^{-3}$
2TiO <sub>2</sub> sol, 1 soot	$5.92 \times 10^{-4}$	$6.13 \times 10^{-4}$	$1.97 \times 10^{-3}$
8TiO <sub>2</sub> sol, 1 soot	$7.54 \times 10^{-4}$	$8.81 \times 10^{-4}$	$3.82 \times 10^{-3}$

screening ( $r_{\text{soot}}/I_{\text{TiO}_2}$ ), where  $I_{\text{TiO}_2}$  changes with UV illumination time. The subscript “max” and “initial” refer to the maximum FQE and the FQE at initial times ( $t = 0$ ), respectively.

$$\phi = \frac{\text{Rate of photocatalyzed reaction (molecules/s)}}{\text{Incident light intensity (photons/s)}} = \left( \frac{r_{\text{soot}}}{I_{\text{soot}}} \right) \text{ or } \left( \frac{r_{\text{soot}}}{I_{\text{TiO}_2}} \right) \quad (9)$$

The maximum FQEs occur at initial times for ( $r_{\text{soot}}/I_{\text{TiO}_2}$ ), and they are all of the same order of magnitude:  $3.5 \times 10^{-3}$  molecules reacted/incident photons. For ( $r_{\text{soot}}/I_{\text{soot}}$ ), the maximum FQEs do not occur at initial times because the reaction rate is slow. The ( $r_{\text{soot}}/I_{\text{soot}}$ )<sub>max</sub> values are comparable to those of ( $r_{\text{soot}}/I_{\text{TiO}_2}), while the ( $r_{\text{soot}}/I_{\text{soot}})<sub>initial</sub> are nearly an order of magnitude smaller than the maximum ( $r_{\text{soot}}/I_{\text{TiO}_2}) values, reflecting considerable light absorption by the soot layer. Mills et al. [7] performed soot PCO experiments using a FTIR gas cell to measure volatile carbonaceous species, such as CO<sub>2</sub>, under 4.28 mW/cm<sup>2</sup> near-UV irradiation and 101.3 kPa O<sub>2</sub> gas flow. They calculated a ( $r_{\text{soot}}/I_{\text{soot}})<sub>initial</sub> FQE of  $1.1 \times 10^{-4}$  molecules/photon, which is similar to our reported ( $r_{\text{soot}}/I_{\text{soot}})<sub>initial</sub>.$$$$$

## 4. Conclusions

Soot photocatalyzed oxidation was studied quantitatively using single- and multi-layer soot and TiO<sub>2</sub> thin films deposited on QCM crystals. Characterization of the sol–gel derived TiO<sub>2</sub> thin films showed (a) low surface roughness; (b) a linear dependence of TiO<sub>2</sub> layer thickness with number of spin coats; and (c) anatase and rutile phase crystallinity. By varying the amount of soot deposited

on the TiO<sub>2</sub>-coated crystals, experiments revealed a range of behaviors from complete mineralization of soot (single and double passes of soot deposition), partial oxidation up to 15,000 min (four deposition passes), and minimal oxidation of soot up to 20,000 min (eight deposition passes) caused by soot screening of the incident UV light. Water vapor adsorption on and/or homogeneous photooxidation of the soot are postulated for the slow increase in  $\Delta m$  for non-photocatalyzed circumstances: 1 soot/no TiO<sub>2</sub> (no photocatalyst), and 8 soot/TiO<sub>2</sub> (opaque soot layer). Varying the TiO<sub>2</sub> thickness did not demonstrate significant changes in the soot destruction rate because oxidation of soot in direct contact with TiO<sub>2</sub> is the dominant reaction compared to lateral and remote soot oxidation, and the soot/TiO<sub>2</sub> contact area is independent of TiO<sub>2</sub> thickness.

The series/parallel reaction mechanism was successfully utilized to describe the PCO reaction kinetics of soot mass loss for  $t > 1000$  min. All three rate constants between each experiment studied were the same order of magnitude. For short times where  $t < 1000$  min, two phenomena appear to have occurred which are not captured by our model: (1) early thermal desorption from TiO<sub>2</sub>/soot surface ( $t < 30$  min); (2) destruction and removal of organic carbons readily accessible and in direct contact to the TiO<sub>2</sub> film ( $t < 1000$  min). We can use the kinetic model to predict the change in the more graphitic  $\Delta m$  as a function of UV illumination time for various soot loadings.

## Acknowledgments

The authors thank the State of North Carolina for funding of this research, North Carolina State University colleagues Yazan A. Hussain (post-doctorate) for advice and general discussion on the quartz crystal microbalance and A. Evren Ozcam (graduate student) for advice on spectroscopic ellipsometry. We also thank Professor Marc A. Anderson and Jennifer Sanfilippo of his University of Wisconsin, Madison, group for advice on the preparation of TiO<sub>2</sub> sol-gel materials.

## References

- [1] Pilkington Glass plc., <http://www.pilkington.com/international+products/activ/> (accessed in 2008).
- [2] Pittsburgh Plate and Glass (PPG), <http://www.ppgsunclean.com/> (accessed in 2008).
- [3] Saint-Gobain Glass, [www.saint-gobain-glass.com/bioclean/](http://www.saint-gobain-glass.com/bioclean/) (accessed in 2008).
- [4] TOTO Limited, <http://www.toto.com.hk/tech/hydratec/index.html> (accessed in 2008).
- [5] MCH Nano Solutions, <http://www.mchnanosolutions.com/index.html> (accessed in 2008).
- [6] N.C. Lee, W.Y. Choi, *Journal of Physical Chemistry B* 106 (2002) 11818.
- [7] A. Mills, J. Wang, M. Crow, *Chemosphere* 64 (2006) 1032.
- [8] S.K. Lee, S. McIntyre, A. Mills, *Journal of Photochemistry and Photobiology A - Chemistry* 162 (2004) 203.
- [9] P. Chin, G.W. Roberts, D.F. Ollis, *Industrial & Engineering Chemistry Research* 46 (2007) 7598.
- [10] R.J. Farrauto, C.H. Bartholomew, *Fundamentals of Industrial Catalytic Processes*, first ed., Blackie Academic & Professional (an imprint of Chapman & Hall), London, UK, 1997.
- [11] R.M. Heck, R.J. Farrauto, S.T. Gulati, *Catalytic Air Pollution Control Commercial Technology*, second ed., John Wiley & Sons, Inc., New York, NY, 2002.
- [12] B.R. Stanmore, J.F. Brilhac, P. Gilot, *Carbon* 39 (2001) 2247.
- [13] G. Neri, L. Bonaccorsi, A. Donato, C. Milone, M.G. Musolino, A.M. Visco, *Applied Catalysis B - Environmental* 11 (1997) 217.
- [14] A.F. Ahlstrom, C.U.I. Odenbrand, *Carbon* 27 (1989) 475.
- [15] A. Messerer, R. Niessner, U. Poschl, *Carbon* 44 (2006) 307.
- [16] C.A. Querini, M.A. Ulla, F. Requejo, J. Soria, U.A. Sedran, E.E. Miro, *Applied Catalysis B - Environmental* 15 (1998) 5.
- [17] Y.Z. Chen, N. Shah, A. Braun, F.E. Huggins, G.P. Huffman, *Energy & Fuels* 19 (2005) 1644.
- [18] A. Braun, N. Shah, F.E. Huggins, K.E. Kelly, A. Sarofim, C. Jacobsen, S. Wirick, H. Francis, J. Ilavsky, G.E. Thomas, G.P. Huffman, *Carbon* 43 (2005) 2588.
- [19] A.M. Nienow, J.T. Roberts, *Annual Review of Physical Chemistry* 57 (2006) 105.
- [20] J.P.A. Neeft, T.X. Nijhuis, E. Smakman, M. Makkee, J.A. Moulijn, *Fuel* 76 (1997) 1129.
- [21] G. de Soete, *Catalysis of soot combustion by metal oxides*, in: Western States sectional meeting, Salt Lake City, 1988.
- [22] P. Darcy, P. Da Costa, H. Mellottee, J.M. Trichard, G. Djega-Mariadassou, *Catalysis Today* 119 (2007) 252.
- [23] A.F. Ahlstrom, C.U.I. Odenbrand, *Applied Catalysis* 60 (1990) 143.
- [24] Q.Y. Xu, M.A. Anderson, *Journal of Materials Research* 6 (1991) 1073.
- [25] N.F. Mott, E.A. Davis, *Electronic Processes in Non-Crystalline Materials*, Oxford University Press, London, 1971.
- [26] C. Lu, A.W. Czanderna, *Applications of Piezoelectric Quartz Crystal Microbalances*, Elsevier Science Publishing Company, Inc., New York, NY, 1984.
- [27] D.X. Wang, P. Mousavi, P.J. Hauser, W. Oxenham, C.S. Grant, *Colloids and Surfaces A - Physicochemical and Engineering Aspects* 268 (2005) 30.
- [28] Y. Hussain, Y.T. Wu, P.J. Ampaw, C.S. Grant, *Journal of Supercritical Fluids* 42 (2007) 255.
- [29] Y.T. Wu, P.J. Akoto-Ampaw, M. Elbaccouch, M.L. Hurrey, S.L. Wallen, C.S. Grant, *Langmuir* 20 (2004) 3665.
- [30] G. Sauerbrey, *Zeitschrift Fur Physik* 155 (1959) 206.
- [31] D.A. Buttry, M.D. Ward, *Chemical Reviews* 92 (1992) 1355.
- [32] H. Muramatsu, A. Egawa, T. Ataka, *Journal of Electroanalytical Chemistry* 388 (1995) 89.
- [33] K.K. Kanazawa, J.G. Gordon, *Analytica Chimica Acta* 175 (1985) 99.
- [34] C.K. O'Sullivan, G.G. Guilbault, *Biosensors & Bioelectronics* 14 (1999) 663.
- [35] M.E. Frerking, *Crystal Oscillator Design and Temperature Compensation*, Van Nostrand Reinhold Company, Inc., New York, NY, 1978.
- [36] Joint Committee on Powder Diffraction Standards, International Centre for Diffraction Data (JCPDS-ICDD), Powder Diffraction File, Swarthmore, PA, 1998.
- [37] H. Choi, A.C. Sofranko, D.D. Dionysiou, *Advanced Functional Materials* 16 (2006) 1067.
- [38] A. Mills, N. Elliott, G. Hill, D. Fallis, J.R. Durrant, R.L. Willis, *Photochemical & Photobiological Sciences* 2 (2003) 591.
- [39] N.P. Mellott, C. Durucan, C.G. Pantano, M. Guglielmi, *Thin Solid Films* 502 (2006) 112.
- [40] E. Stathatos, H. Choi, D.D. Dionysiou, *Environmental Engineering Science* 24 (2007) 13.
- [41] R. Fretwell, P. Douglas, *Journal of Photochemistry and Photobiology A - Chemistry* 143 (2001) 229.
- [42] X.Z. Fu, W.A. Zeltner, Q. Yang, M.A. Anderson, *Journal of Catalysis* 168 (1997) 482.
- [43] O. Carp, C.L. Huisman, A. Reller, *Progress in Solid State Chemistry* 32 (2004) 33.
- [44] D. Ferry, J. Suzanne, S. Nitsche, O.B. Popovitcheva, N.K. Shonija, *Journal of Geophysical Research - Atmospheres* 107 (2002).
- [45] B.V. Kuznetsov, T.A. Rakhmanova, O.B. Popovitcheva, N.K. Shonija, *Journal of Aerosol Science* 34 (2003) 1465.
- [46] O.B. Popovitcheva, N.M. Persiantseva, M.E. Trukhin, G.B. Rulev, N.K. Shonija, Y.Y. Buriko, A.M. Starik, B. Demirdjian, D. Ferry, J. Suzanne, *Physical Chemistry Chemical Physics* 2 (2000) 4421.
- [47] A.R. Chughtai, G.R. Williams, M.M.O. Atteya, N.J. Miller, D.M. Smith, *Atmospheric Environment* 33 (1999) 2679.
- [48] E.A. Muller, L.F. Rull, L.F. Vega, K.E. Gubbins, *Journal of Physical Chemistry* 100 (1996) 1189.
- [49] J.K. Brennan, K.T. Thomson, K.E. Gubbins, *Langmuir* 18 (2002) 5438.
- [50] N. Grassie, G. Scott, *Polymer Degradation & Stabilization*, Cambridge University Press, New York, NY, 1985.
- [51] W. Kubo, T. Tatsuma, A. Fujishima, H. Kobayashi, *Journal of Physical Chemistry B* 108 (2004) 3005.
- [52] H. Haick, Y. Paz, *Chemphyschem* 4 (2003) 617.
- [53] A. Mills, J.S. Wang, M. Crow, G. Taglioni, L. Novella, *Journal of Photochemistry and Photobiology A - Chemistry* 187 (2007) 370.
- [54] A. Mills, J.S. Wang, *Journal of Photochemistry and Photobiology A - Chemistry* 182 (2006) 181.
- [55] S. Sitkiewitz, A. Heller, *New Journal of Chemistry* 20 (1996) 233.
- [56] V. Romeas, P. Pichat, C. Guillard, T. Chopin, C. Lehaut, *New Journal of Chemistry* 23 (1999) 365.
- [57] V. Romeas, P. Pichat, C. Guillard, T. Chopin, C. Lehaut, *Industrial & Engineering Chemistry Research* 38 (1999) 3878.
- [58] P. Chin, D.F. Ollis, *Catalysis Today* 123 (2007) 177.
- [59] P. Chin, L.P. Yang, D.F. Ollis, *Journal of Catalysis* 237 (2006) 29.